Novel strategies for the characterization of cancellous bone morphology: virtual isolation and analysis

Alessio Veneziano[1], Marine Cazenave[2,3], Fabio Alfieri[4,5], Daniele Panetta[6], Damiano Marchi[7,8]

1 Synchrotron Radiation for Medical Physics (SYRMEP), Elettra-Sincrotrone Trieste S.C.p.A., Basovizza, Trieste, Italy
2 Skeletal Biology Research Centre at the School of Anthropology and Conservation, University of Kent, Canterbury, UK
3 Department of Anatomy and Histology, Sefako Makgatho Health Sciences University, Pretoria, South Africa
4 Institut für Biologie, Humboldt Universität zu Berlin, Berlin, Germany.
5 Museum für Naturkunde, Leibniz-Institut für Evolutions- und Biodiversitätsforschung, Berlin, Germany
6 Istituto di Fisiologia Clinica, Consiglio Nazionale delle Ricerche (CNR), Pisa, Italy
7 Department of Biology, Università di Pisa, Pisa, Italy
8 Evolutionary Studies Institute and Centre for Excellence in PalaeoSciences, University of the Witwatersrand, Johannesburg, South Africa
Corresponding Author: Alessio Veneziano

ABSTRACT

Objectives: The advent of micro-computed tomography (µCT) made cancellous bone more accessible than ever before. Nevertheless, the study of cancellous bone is hindered by its inherent complexity and the difficulties linked to defining homology across datasets. Here we propose novel virtual methodological approaches to overcome those issues and complement existing methods.

Materials and methods: We present a protocol for the semi-automatic isolation of the whole cancellous region within a µCT scanned bone. This method overcomes the subsampling issues and allows studying cancellous bone as a single unit. We test the protocol on a set of primate bones. Also, we describe a set of morphological indices calculated on the topological skeleton of the cancellous bone: node density, node connectivity, trabecular angle, trabecular tortuosity and fractal dimension. The usage of the indices is shown on a small comparative sample of primate femoral heads.

Results: The isolation protocol proves reliable in isolating cancellous structures from several different bones, regardless of their shape. Most of the indices seem to detect differences due to locomotion and bone use, thus highlighting their potential in the study of cancellous architecture.

Discussion: The approaches presented overcome some of the difficulties of trabecular bone studies. Our analysis also suggests that the indices calculated on the topological skeleton have high potential to detect functional signals in the cancellous bone. The methods presented here represent an alternative or supporting method to the existing tools available to address the biomechanics of cancellous bone.

Keywords: Bone segmentation; trabecular architecture; bone complexity; skeletonization; primates

1 INTRODUCTION

Besides the influence of metabolic factors and the genetic imprint on the inner bone organization, the bone tissues modeled during life to adjust to the loading environment. Growing evidence suggests that cancellous bone is responsive to variations in nature, direction, frequency and magnitude of load throughout life (Carter, Orr & Fyhrie, 1989; Goldstein, Matthews, Kuhn & Hollister, 1991; Huiskes, Ruimerman, Van Lenthe & Janssen, 2000; Kivell, 2016; Macchiarelli, Bondioli, Galichon & Tobias, 1999; Rafferty & Ruff, 1994), thus reflecting directly how a joint or bone was used. Also, trabecular morphology has been observed to vary in response to nutrient intake (Chen et al., 2002; Gunnes & Lehmann, 1995, 1996; Tu et al., 2007) and hormones (Andreassen & Oxlund, 2001; Miyakoshi, 2004). Therefore, research has turned to cancellous bone to address issues of bone usage, biomechanics and stress in forensic (Villa, Hansen, Buckberry, Cattaneo & Lynnerup, 2013) and biological anthropology (Cazenave et al., 2019; Georgiou, Kivell, Pahr, Buck & Skinner, 2019; Macchiarelli et al., 1999; Rafferty & Ruff, 1994; Ryan & Shaw, 2012; Scherf, Harvati & Hublin, 2013; Tsegai, Skinner, Pahr, Hublin & Kivell, 2018a), archaeology (Bishop, Clemente, Hocknull, Barrett & Lloyd, 2017; Kneissel et al., 1994; Scherf, Wahl, Hublin & Harvati, 2016) and paleontology (Bishop et al., 2017, 2018; Sinclair et al., 2013). The advent of high-resolution X-ray and micro-Computed Tomography (µCT) expanded the methodological horizons of cancellous bone studies as they made bone internal structures non-invasively accessible (Fajardo, Ryan & Kappelman, 2002) and allowed the virtual manipulation of cancellous bone (Odgaard, 1997). Besides, the non-invasive nature of µCT extended the analysis of cancellous bone to fragile and unique specimens, a condition rather common in studies relying on museum collections or fossil specimens (Conroy & Vannier, 1984; Witmer, Ridgely, Dufeau & Semones, 2008).

Cancellous bone is composed of trabecular elements intertwined with each other to form an intricate structure with no analogy to regular solid shapes and, therefore, hard to describe through traditional morphometrics (Hildebrand, Laib, Müller, Dequeker & Rüegsegger, 1999; Odgaard, 1997). Furthermore, the developing trabecular lattice responds to endogenous and exogenous factors, and it is modeled throughout life by the complex interaction between those factors (Cooper, 1990; Little, Rogers & Flannery, 2011). Although numerous studies focused on trabecular architecture, the characterization of cancellous bone morphology has been hindered by its inherent complexity.

Previous work focused on small subsamples of the trabecular network to reduce cancellous complexity and analyze it (Fajardo & Müller, 2001; Moon et al., 2004; Räth et al., 2008; Ryan & Ketcham, 2002). Such regions are usually isolated manually after orienting the tomographic volume. Unfortunately, the subsamples bear only local information while several regions or large subsamples are needed to account for the three-dimensional variations of the trabecular properties across the bone. Also, the position and orientation of those regions are difficult to define univocally. Therefore, the choice of the local region under analysis may bias the results (Fajardo & Müller, 2001; Lazenby, Skinner, Kivell & Hublin, 2011). As a result, there exist intrinsic ambiguities in defining anatomical homology between trabecular regions in intra- and inter-specific studies. Nevertheless, studies showed that additional functional information can be obtained by analyzing the whole cancellous bone within the epiphysis (Georgiou et al., 2019; Sylvester & Terhune, 2017; Tsegai et al., 2013; Tsegai, Skinner, Pahr, Hublin & Kivell, 2018b).

In summary, the study of cancellous bone can be hindered by (I) its inherent complexity and (II) the difficulties associated with isolating homologous cancellous regions. In this work we address both issues. First, we present a reproducible protocol for isolating cancellous structures from µCT images and volumes, thus allowing the analysis of cancellous regions as single units and without subsampling. Second, we present a set of indices for the quantification of complexity measured on the topology of the cancellous structure. Finally, we discuss these newly introduced methods in the light of existing techniques, the novelty they introduce and their potential to identify functional signals in cancellous structures.

2 MATERIALS AND METHODS

2.1 Automatic isolation of cancellous bone

We designed a protocol for the semi-automatic isolation of cancellous bone from µCT images and volumes. The isolation procedure works on binary images (black and white) of the skeletal region of interest, therefore some preliminary steps are required to transform the µCT data suitably. The µCT of the bone is cropped to include only the region under investigation, oriented according to the user's needs. Image binarization can be achieved via image segmentation methods (Pham, Xu & Prince, 2000). The binarization returns images exhibiting the bone and the background only, respectively as white and black pixels.

The protocol relies on the combination of the image processing operators "Dilation" and "Erosion" (Serra, 1982; Urbach & Wikinson, 2007), which respectively enlarge and shrink features in binary images according to a pattern specified by a structuring element. Structuring elements are matrices of odd dimensions that identify the pixel in the image being processed (Urbach & Wikinson, 2007). Each pixel in the image is the center of the structuring element. The neighboring pixels are the cells of the element that surround its center. Each pixel is modified based on the value of its surrounding pixels, accordingly to the pattern in the structuring element. In the case of dilation and erosion, each white pixel (region of interest) in the image will grow and shrink over its neighboring pixels in the fashion specified by the values in the structuring element. Size and shape of the structuring element vary with regards to the image to be processed and the desired result. The process performed by the operator-structuring element system is illustrated in the supplementary information (Figure S1).

The protocol consists of five sequential operations alternating dilation/erosion to subtractions between images and it is applied sequentially on all the slices constituting the µCT scan. The number of iterations for dilation/erosion differ for each operation and depends on the cross-sectional morphology of the bone to be segmented and on the size of the structuring element. Larger structuring elements provide finer dilations and erosions, although these effects can be detrimental in low-resolution images. In fact, the structuring element defines the size and direction of image transformations. Therefore, large structuring elements applied to low-resolution images can close small holes (dilation) or erase small elements (erosion) represented by fewer pixels than it would be in high-resolution images.

Figure 1 illustrates the operations for a single 2D image. (Step 1) The white pixels of the binary image (B) initially undergo multiple dilations that fill the empty spaces within the bone; the same amount of erosions is then applied to shrink the bone back to its original size and external contours. The result is a mask (C) identifying the region occupied by cancellous bone, compact bone and voids. (Step 2) The subtraction between the pixels of the binary image and the ones of the mask (B – C) provides a new image where only the voids are represented (D). (Step 3) Multiple dilations of the voids close the spaces occupied by trabecular structures and erosions restore its size and external contours. The white pixels of the resulting image occupy the internal region of the bone (E), the space hosting cancellous bone and voids. (Step 4) The internal region is then subtracted from the mask (C – E), thus isolating the compact bone (F). (Step 5) The cancellous bone (G) is finally obtained by subtracting the voids and the compact bone from the mask (C – D – F). The three-dimensional result of the protocol is shown in Figure 1. The protocol was developed in the R programming environment (R Core Team, 2019). The operations of dilation and erosion are performed using the package “EBImage” (Pau, Fuchs, Sklyar, Boutros & Huber, 2010). All other operations use basic R coding.

[Figure 1]

2.2 Indices of cancellous complexity

To extract descriptive information of cancellous architecture and complexity, the isolated cancellous volumes are processed through skeletonization. This operation returns the minimal geometric descriptor of an image, usually referred to as “topological skeleton”, by reducing it to a set of connected nodes and branches (Zhou & Toga, 1999) (Supplementary information, Figure S2). The resulting skeleton retains topology and shape of the cancellous lattice. In the cancellous bone, branches represent the trabeculae while nodes are their extremes as well as the points of connection between contiguous trabeculae. The nodes and branches of each skeleton are then processed in R for calculating five indices: node density, trabecular angle, trabecular connectivity, trabecular tortuosity and fractal dimension. A graphical representation of these measurements is illustrated in Figure 2, where skeletonization is represented in 2D just for ease of visualization. The actual skeletonization and calculation of indices are instead performed in 3D.

Node density is the three-dimensional spatial density of skeleton nodes which is a proxy for trabecular spatial density and the relative proximity of trabecular connections. It is measured using a kernel density approximation (Venables & Ripley, 2002) over a regular 3D grid and it is expressed as number of nodes per cm^3. To reduce the effect of size on the calculation of spatial node density, the 3D coordinates of the skeleton nodes are scaled on their variance.

Trabecular angle is the 3D angle in degrees between a reference axis and the unitary resultant of all trabecular directions obtained by vector sum in 3D. The direction of single trabeculae is calculated as the difference between the starting and ending nodes of each branch in x, y and z.

Trabecular connectivity is measured as the mean number of branches connected to each node of the skeleton. Only nodes with at least two connections (non-terminal nodes) are considered to calculate the average.

Trabecular tortuosity is the ratio between the arc length of a branch and the linear distance between its starting and ending nodes (Roque & Alberich-Bayarri, 2015). Tortuosity measures the degree of trabecular curvature and runs from 1 (straight trabeculae) to, theoretically, infinity. It describes the sinuosity of singular trabecular units and it is known to increase with decreasing stiffness (Roque & Alberich-Bayarri, 2015). Because tortuosity is the ratio between two lengths, it is dimensionless.

Fractal dimension is an index of complexity. It measures the change in detail over different scales of observation (Falconer, 2004). The rationale of fractal dimension is that more complex features present more details at finer scales. Fractal dimension is here measured on the 3D coordinates of the skeleton branches using the box-counting algorithm (Annadhason, 2012). In this approach, 3D grids of decreasing cell size (decreasing cell side length, increasing number of cells) are superimposed over the cancellous skeleton. The number of cells overlapping the structure are counted for each subsequent grid: the fractal dimension is the slope of the line fitting the number of cells that overlap the skeleton versus the inverse of the cell size. The cell size over subsequent grid is here decreased linearly. To avoid the effect of the size of the cancellous region, the 3D coordinates of the skeleton branches should be scaled.

[Figure 2]

2.3 Application of the isolation protocol and complexity indices

To show the results of the protocol for cancellous isolation, we use µCT scans of five skeletal regions from five species of primates: the mandibular condyle, the brow ridge, the humerus, the femur and the fibula. Additional details about the specimens are reported in the supplementary information (Table S1). Prior to the application of the protocol, the µCT scans are cropped to isolate the region of interest and binarized using Otsu thresholding (Otsu, 1979; Vala & Baxi, 2013).

The usage of complexity indices is shown for a small comparative sample of µCT scanned femoral heads of specimens belonging to seven species of catarrhine primates. Additional details are reported in the supplementary information (Table S2). The aim is to demonstrate the usage, feasibility and interpretation of the indices in comparative analyses and functional frameworks. Each femoral head is cropped and binarized using Otsu thresholding, and the cancellous bone was isolated using the protocol described above. The segmented cancellous regions underwent skeletonization using the Amira 5.4.5 software package (FEI Visualization). The indices were then measured in the R environment using the 3D coordinates of nodes and branches constituting the skeletonized cancellous bone.

3 RESULTS

3.1 Cancellous bone isolation

The dilation and erosion operators were applied on every slice of each binarized μCT using a circular, 5x5 pixels structuring element. The number of dilation and erosions varied at each step and across bones depending on image size and, therefore, on the image resolution. For all the bones, the number of iterations at each step never exceeded six erosions and dilations. In all bones, the application of the protocol returned the cancellous lattice with little to negligible areas of the compact bone left attached (Supplementary information, Figure S3). The 2D and 3D results for the mandibular condyle are shown in Figure 1, where this region is used to present the steps of the protocol. For the other skeletal regions, the results are shown in Figure 3.

[Figure 3]

3.2 Node density in the comparative sample

Summary statistics of the complexity indices for the specimens analyzed are detailed in Table 1. *Pan*, *Gorilla* and humans exhibit an average (47.89 ± 15.84, 40.51 ± 16.52 and 45.51 ± 14.93 nodes per cm^3) and maximum (472.69, 503.97 and 557.71 nodes per cm^3) density, higher than that observed in *Macaca* (mean: 39.38 ± 17.1; max.: 238.91), *Papio* (mean: 38.81 ± 15.32; max.: 289.09), *Hylobates* (mean: 37.99 ± 13.12; max.: 150.73) and *Symphalangus* (mean: 36.93 ± 14.19; max.: 228.75). *Hylobates* and *Symphalangus* exhibit the lowest density values in the sample. However, note the high variability of node density from the mean value in all specimens (Table 1).

The color maps (Figure 4) confirm high node density for humans and *Pan*, although more localized toward the head's perimeter in the former while more widespread in the latter. In coronal view, two regions of higher node density are observed in humans. The first runs from the supero-lateral region to the inferior aspect of the femoral head and the other extends from the superior to the medial region of the head, adjoining the surface. In para-sagittal view, a denser region is found connecting the inferior surface, while the center of the head shows the lower node density. *Gorilla* exhibits very concentrated zone of higher node density compared to both *Pan* and humans. In coronal view, *Gorilla* shows a region of higher trabecular density extending supero-inferiorly in the lateral aspect of the head, as well as a denser region in the medial aspect at the level of the fovea capitis. In the para-sagittal view, we observe higher node densities in the supero-anterior region and infero-posteriorly. In coronal view, *Macaca* and *Papio* show a dense region extending from the supero-lateral to the inferior aspect of the head and corresponding to the arcuate bundle. Such dense region is well visible inferiorly in the para-sagittal view of *Papio*, while, in *Macaca*, higher densities are more dispersed across antero-inferiorly. The coronal and para-sagittal views in *Hylobates* and *Symphalangus* show lower node densities more dispersed across the femoral head than in other species.

[Figure 4]

3.3 Trabecular angle, connectivity, tortuosity and fractal dimension

The trabecular angle measured on the femoral head was referenced onto the medio-lateral axis. Figure 5 shows the resultant direction of the trabeculae for each specimen and the angles are reported in Table 1. All angles are oriented medio-laterally with only minor departures from the reference axis. *Pan* and *Hylobates* exhibit the largest angles (α: 12.2° and 11.6° respectively) with the main direction running medio-laterally with a minimal anteroposterior contribution. Similarly, *Gorilla* displays medio-lateral trabecular direction angled at 7.4° with minor antero-posterior contribution. *Macaca*, *Symphalangus*, humans and *Papio* exhibit lower angles (α: 5.7°, 4.9°, 4.6° and 2.8° respectively), with medio-lateral contributions being far more represented than the anteroposterior and the supero-inferior ones.

Mean trabecular connectivity is larger in humans and *Pan* (3.86 ± 1.29 and 3.81 ± 1.19, respectively) than in the other specimens (Table 1). The femoral head of *Gorilla* shows an average of 3.53 ± 0.95

branches per node, followed by *Papio* (3.49 ± 0.86), and *Macaca* (3.38 ± 0.78). *Symphalangus* (3.28 ± 0.68) and *Hylobates* (3.22 ± 0.58) exhibit the lowest mean connectivity in the sample.

For what concerns tortuosity (Table 1), *Macaca* exhibits the lowest mean values (1.11 ± 0.19), which is instead higher in *Papio* (1.23 ± 0.25). In *Pan* (1.18 ± 0.17), humans (1.21 ± 0.21) and *Gorilla* (1.23 ± 0.24), mean tortuosity is larger than in *Macaca* but comparable to *Papio*. The highest tortuosity in the sample is displayed by the gibbons. *Hylobates* and *Symphalangus* show 1.29 ± 0.36 and 1.26 ± 0.31 mean tortuosity, respectively.

Fractal dimension was calculated for the original and scaled topological skeletons. For scaling, we used the height of the femoral head. For *Pan* and humans (Table 1) this index is higher than in all other specimens (2.62 and 2.63 respectively, 2.53 and 2.51 when scaled), followed by *Gorilla* (2.55, scaled 2.47), *Macaca* (2.49, scaled 2.42) and *Papio* (2.47, scaled 2.39). *Hylobates* (2.32, scaled 2.3) and *Symphalangus* (2.41, scaled 2.37) show the lowest fractal dimensions.

[Figure 5]

[Table 1]

4 DISCUSSION

The study of cancellous architecture promises to clarify biomechanical, evolutionary and physiological aspects of the human and vertebrate skeleton. Because of the multiple aspects involved in shaping cancellous bone architecture, a better understanding of its variability may have important effects on fields such as evolutionary and biological anthropology, paleontology and medicine. The characterization of cancellous morphology is made difficult by the lack of anatomical/functional homology when studying subsamples and the inherent complexity of the structure. This paper introduces novel approaches to the study of cancellous bone by presenting the usage of a new method for isolating trabecular structures in µCT scans and a set of complexity indices measured on the topological skeleton of the cancellous bone.

4.1 Cancellous isolation without subsampling

The protocol presented in this paper provides a flexible way of separating the cancellous bone from the compact bone thanks to the sequential application of image processing operators. Its flexibility is based on the possibility to change the number of dilations/erosions performed at each step of the procedure as well as the size and shape of the structuring element. These parameters are necessary because µCT scans come in different resolutions and bones come in different proportions of compact to cancellous bone as well as different shapes. The possibility to refine the procedure allows adapting the protocol to several cases. Changes in the shape of structuring element, for example, allow performing dilations and erosions accordingly to the cross-sectional shape of the bone, therefore reducing the loss due to the irreversibility of the operators. Figure 3 demonstrates the usefulness and potential of the protocol on different bones. The isolated cancellous region is well separated from the compact bone and ready for further analysis.

4.2 Cancellous topology and complexity indices

Several tools are available to study the morphology of cancellous regions in terms of trabecular direction, shape, separation, thickness and more (Fajardo & Müller, 2001; Odgaard, 1997). The indices used in this paper do not aim to substitute those tools but rather to complement them. In fact, many algorithms for the characterization of cancellous architecture measure indices directly on the µCT images. The approach we present in this work relies on the reduction of the cancellous shape to its minimal descriptor: the topological skeleton. The skeletonization process is known to enhance certain geometrical and topological aspects of a shape, such as connectivity, length and direction (Davies, 2004). Therefore, measuring indices of connectivity, tortuosity, density and, overall, complexity on the topological skeleton of the cancellous bone can be advantageous.

Node density has been mainly used to address bone response to osteoporosis (Chappard, Alexandre & Riffat, 1988) rather than bone mechanical properties. Here, it represents the number of trabeculae per unit volume. The link between node density and function is straightforward: higher stress is counteracted by higher density of connections between trabeculae. Our results suggest that node density in the femoral head could reflect differences in loads during locomotion. In fact, the posture and locomotion of modern humans (bipedal), *P. troglodytes* and *G. gorilla* (knuckle-walkers) produces higher mechanical load (body weight) on the hind limbs than in quadrupedal mammals (Druelle, Berthet & Quintard, 2019; Raichlen, Shapiro, Pontzer & Sockol, 2009). These species present the highest node densities in the sample analyzed here, although the high variability of the estimation suggests that the local distribution of density is more important than the overall statistics. In hylobatids, node density appears lower and more dispersed across the femoral head than in other primates, probably as a result of relying mostly on forelimbs for brachiation (Preuschoft, Schönwasser & Witzel, 2016). High density regions in *Macaca* and *Papio* seem to extend along the arcuate bundle, thus suggesting the significance of node density for bone biomechanics.

Connectivity has been measured via multiple approaches (Ding, Odgaard, Linde & Hvid, 2002; Kabel, Odgaard, Van Rietbergen & Huiskes, 1999; Odgaard & Gundersen, 1993). Here we simplify those approaches by simply counting the average number of branches of the topological skeleton connected to the same node. Higher connectivity can be expected when cancellous structures are subject to large loads because more connections and more trabeculae allow to spread the load over a wider surface, thus releasing stress on localized areas (Silva & Gibson, 1997). Our results on the comparative sample suggest that the average number of connections per node could inform about function. Indeed, species whose locomotion privileges higher loads on the hind limbs (humans) exhibit the highest average connectivity, while the group which privileges the use of forelimb during habitual locomotion (hylobatids) exhibits the lowest average connectivity.

Trabecular tortuosity has been recognized as a promising indicator of the mechanical behavior of cancellous bone (Roque & Alberich-Bayarri, 2015). More sinuous, convoluted trabeculae are associated to decreased stiffness (Roque & Alberich-Bayarri, 2015; Roque, Arcaro & Lanfredi, 2012). Therefore, tortuosity reflects flexibility when the bone is subject to load. Our results support this association because the highest tortuosity was found in hylobatids, which exhibit a broad set of locomotor behaviors involving both hind and forelimbs (Fleagle, 2013). This variegated locomotion might need accommodating highly variable loads on the hind limbs, rather than the predictable stress of a cycled gait. This is also reflected in the lowest value observed in *Macaca*, which are involved in the more conservative way of locomotion (quadrupedalism) (Ryan & Shaw, 2012) among primates.

The idea behind trabecular angle is that the main direction of trabeculae could detect the trajectory of the principal stress due to locomotion (Hayes & Snyder, 1981). Our results are controversial and hard to interpret. No substantial or meaningful differences are highlighted in the sample. Despite the consistency of our results, it is not possible to exclude that the resultant trabecular direction has actually detected the principal stress trajectory, which could direct the load stress medio-laterally. Further analyses are needed to verify the potential of trabecular angle.

Fractal dimension measured on µCT images or radiographs has been previously applied to the study of cancellous bone in both medical and osteological works (Fazzalari & Parkinson, 1997; Feltrin, Stramare, Miotto, Giacomini & Saccavini, 2004; Haire, Hodgskinson, Ganney & Langton, 1998; Messent, Ward, Tonkin & Buckland-Wright, 2005). The rationale behind fractal dimension is that more complex cancellous structures are more interconnected, which allows spreading the load over a wider surface (Silva & Gibson, 1997). Here we measure fractal dimension on the topological skeleton rather than on µCT volumes or radiographic images. By reducing the cancellous architecture to its minimal descriptor, we are excluding factors exhibiting local variation (such as trabecular thickness) from the measurements. Therefore, the fractal dimension proposed here is only analogous to what used previously in literature. In our approach, fractal dimension is a measure of the cancellous lattice complexity and enhances the importance of connection between trabeculae. Based on the results on the comparative sample, fractal dimension seems to detect a signal related to limb use. In fact, the lowest values of fractal dimension are exhibited by *Hylobates* and *Symphalangus*, whose arboreal lifestyle relies consistently on the forelimbs. *Papio* and *Macaca* show values in between those of hylobatids and the great apes here analyzed. These results may indicate that higher cancellous complexity in the femoral head is required to counteract higher loads during locomotion.

ACKNOWLEDGEMENTS

The authors wish to thank the curators at the various museum and institutions where data were collected. For the primate fibula we want to thank the Natural History Museum “La Specola” in Florence (Italy). For access to the primate femora, we are grateful to the curatorial staff of the Department of Anatomy of the University of Pretoria (South Africa); the Department of Anatomy and Histology of the Sefako Makgatho Health Sciences University (South Africa); the Evolutionary Studies Institute of the University of the Witwatersrand (South Africa); the Museum of Comparative Zoology of the Harvard University (USA); the Primate Research Institute of Kyoto University (Japan); the R.A. Dart Collection of the University of the Witwatersrand (South Africa); the Smithsonian National Museum of Natural History (USA); the American Museum of Natural History (USA). For scanning, we thank the staff the microfocus X-ray tomography facility of the Center for Nanoscale Systems (CNS) of the Harvard

University, Cambridge (USA); the Evolutionary Studies Institute of the University of the Witwatersrand, Johannesburg (South Africa); the Smithsonian National Museum of Natural History, Washington (USA); the South African Nuclear Energy Corporation SOC Ltd (Necsa), Pelindaba (South Africa); the X-ray synchrotron radiation micro-tomography (SR-µXCT) at the beamline ID 17 of the European Synchrotron Radiation Facility (ESRF), Grenoble (France). We especially acknowledge P. Agnelli (Florence), F. de Beer (Pelindaba), B. Billing (Johannesburg), A. Bravin (Grenoble), J. Hoffman (Pelindaba), K. Jakata (Johannesburg), E. L'Abbé (Pretoria), R. Macchiarelli (Poitiers & Paris), A. Mazurier (Poitiers), M. Nakatsukasa (Kyoto), C. Nemoz (Grenoble), A. Oettlé, (Pretoria), M. Pina (Manchester), T. Ryan (Pennsylvania), P. Tafforeau (Grenoble), and B. Zipfel (Johannesburg). For scientific collaboration and discussion, we thank R. Macchiarelli (Poitiers; Paris), P. Sardini (Poitiers), and C. Zanolli (Bordeaux). M.C. was funded by the Erasmus Mundus programme, Bakeng se Afrika (Sefako Makgatho Health Sciences University, South Africa) and by the postdoctoral allocation from the Fyssen Foundation.

REFERENCES

Andreassen, T. T., & Oxlund, H. (2001). The effects of growth hormone on compact and cancellous bone. *Journal of Musculoskeletal and Neuronal Interactions*, *2*(1), 49-58.

Annadhason, A. (2012). Methods of fractal dimension computation. *International Journal of Computer Science and Information Technology & Security*. 2(1), 166–169

Bishop, P. J., Clemente, C. J., Hocknull, S. A., Barrett, R. S., & Lloyd, D. G. (2017). The effects of cracks on the quantification of the cancellous bone fabric tensor in fossil and archaeological specimens: a simulation study. *Journal of anatomy*, *230*(3), 461-470. https://doi.org/10.1111/joa.12569

Bishop, P. J., Hocknull, S. A., Clemente, C. J., Hutchinson, J. R., Farke, A. A., Barrett, R. S., & Lloyd, D. G. (2018). Cancellous bone and theropod dinosaur locomotion. Part III—Inferring posture and locomotor biomechanics in extinct theropods, and its evolution on the line to birds. *PeerJ*, *6*, e5777. https://doi.org/10.7717/peerj.5777

Carter, D. R., Orr, T. E., & Fyhrie, D. P. (1989). Relationships between loading history and femoral cancellous bone architecture. *Journal of Biomechanics*, *22*(3), 231-244. https://doi.org/10.1016/0021-9290(89)90091-2

Cazenave, M., Oettlé, A., Thackeray, J. F., Nakatsukasa, M., De Beer, F., Hoffman, J., & Macchiarelli, R. (2019). The SKX 1084 hominin patella from Swartkrans Member 2, South Africa: An integrated analysis of its outer morphology and inner structure. *Comptes Rendus Palevol*, 18(2), 223-235.

Chappard, D., Alexandre, C., & Riffat, G. (1988). Spatial distribution of trabeculae in iliac bone from 145 osteoporotic females. *Acta Anatomica*, 132(2), 137-142. https://doi.org/10.1159/000146565

Chen, H., Hayakawa, D., Emura, S., Ozawa, Y., Okumura, T., & Shoumura, S. (2002). Effect of low or high dietary calcium on the morphology of the rat femur. *Histology and histopathology*, *17*(4), 1129-1136. https://doi.org/10.14670/HH-17.1129

Conroy, G. C., & Vannier, M. W. (1984). Noninvasive three-dimensional computer imaging of matrix-filled fossil skulls by high-resolution computed tomography. *Science*, *226*(4673), 456-458. https://doi.org/10.1126/science.226.4673.456

Cooper, C. (1990). Bone mass throughout life: bone growth and involution. In: Francis R. M., Dick W.C. (Eds) *Osteoporosis* (pp. 1-26). Springer, Dordrecht.

Davies, E. R., (2004). *Machine Vision: Theory, Algorithms and Practicalities*. Third Edition. Morgan Kaufmann Publishers, San Francisco, USA.

Ding, M., Odgaard, A., Linde, F., & Hvid, I. (2002). Age-related variations in the microstructure of human tibial cancellous bone. *Journal of Orthopaedic Research*, 20(3), 615-621. https://doi.org/10.1016/S0736-0266(01)00132-2

Druelle, F., Berthet, M., & Quintard, B. (2019). The body center of mass in primates: Is it more caudal than in other quadrupedal mammals? *American journal of physical anthropology*, 169(1), 170-178. https://doi.org/10.1002/ajpa.23813

Fajardo, R. J., & Müller, R. (2001). Three-dimensional analysis of nonhuman primate trabecular architecture using micro-computed tomography. *American Journal of Physical Anthropology*, *115*(4), 327-336. https://doi.org/10.1002/ajpa.1089

Fajardo, R. J., Ryan, T. M., & Kappelman, J. (2002). Assessing the accuracy of high-resolution X-ray computed tomography of primate trabecular bone by comparisons with histological sections. *American Journal of Physical Anthropology: The Official Publication of the American Association of Physical Anthropologists*, *118*(1), 1-10. https://doi.org/10.1002/ajpa.10086

Falconer, K. (2004). *Fractal geometry: mathematical foundations and applications*. Second Edition, Wiley, Chichester

Fazzalari, N. L., & Parkinson, I. H. (1997). Fractal properties of subchondral cancellous bone in severe osteoarthritis of the hip. *Journal of Bone and Mineral Research*, *12*(4), 632-640. https://doi.org/10.1359/jbmr.1997.12.4.632

Feltrin, G. P., Stramare, R., Miotto, D., Giacomini, D., & Saccavini, C. (2004). Bone fractal analysis. *Current osteoporosis reports*, 2(2), 53-58. https://doi.org/10.1007/s11914-004-0004-4

Fleagle, J. G. (2013). *Primate adaptation and evolution*. Third edition. Academic press, New York

Georgiou, L., Kivell, T. L., Pahr, D. H., Buck, L. T., & Skinner, M. M. (2019). Trabecular architecture of the great ape and human femoral head. *Journal of anatomy*, *234*(5), 679-693. https://doi.org/10.1111/joa.12957

Goldstein, S. A., Matthews, L. S., Kuhn, J. L., & Hollister, S. J. (1991). Trabecular bone remodeling: an experimental model. *Journal of biomechanics*, *24*, 135-150. https://doi.org/10.1016/0021-9290(91)90384-Y

Gunnes, M., & Lehmann, E. H. (1995). Dietary calcium, saturated fat, fiber and vitamin C as predictors of forearm compact and trabecular bone mineral density in healthy children and adolescents. *Acta Paediatrica*, *84*(4), 388-392. https://doi.org/10.1111/j.1651-2227.1995.tb13656.x

Gunnes, M., & Lehmann, E. H. (1996). Physical activity and dietary constituents as predictors of forearm compact and trabecular bone gain in healthy children and adolescents: a prospective study. *Acta Paediatrica*, *85*(1), 19-25. https://doi.org/10.1111/j.1651-2227.1996.tb13884.x

Haire, T. J., Hodgskinson, R., Ganney, P. S., & Langton, C. M. (1998). A comparison of porosity, fabric and fractal dimension as predictors of the Young's modulus of equine cancellous bone. *Medical engineering & physics*, *20*(8), 588-593. https://doi.org/10.1016/S1350-4533(98)00063-0

Hayes, W. C., & Snyder B., (1981). Toward a quantitative formulation of Wolff's law in trabecular bone. In: Cowin, S. C. (Ed.), *Mechanical Properties of Bone*. Series AMD, Vol. 45, (pp. 43–68). American Society of Mechanical Engineers, New York

Hildebrand, T., Laib, A., Müller, R., Dequeker, J., & Rüegsegger, P. (1999). Direct three-dimensional morphometric analysis of human cancellous bone: microstructural data from spine, femur, iliac crest, and calcaneus. *Journal of bone and mineral research*, *14*(7), 1167-1174. https://doi.org/10.1359/jbmr.1999.14.7.1167

Huiskes, R., Ruimerman, R., Van Lenthe, G. H., & Janssen, J. D. (2000). Effects of mechanical forces on maintenance and adaptation of form in trabecular bone. *Nature*, *405*(6787), 704-706. https://doi.org/10.1038/35015116

Kabel, J., Odgaard, A., Van Rietbergen, B., & Huiskes, R. (1999). Connectivity and the elastic properties of cancellous bone. *Bone*, 24(2), 115-120. https://doi.org/10.1016/S8756-3282(98)00164-1

Kivell, T. L. (2016). A review of trabecular bone functional adaptation: what have we learned from trabecular analyses in extant hominoids and what can we apply to fossils? *Journal of Anatomy*, *228*(4), 569-594. https://doi.org/10.1111/joa.12446

Kneissel, M., Boyde, A., Hahn, M., Teschler-Nicola, M., Kalchhauser, G., & Plenk Jr, H. (1994). Age-and sex-dependent cancellous bone changes in a 4000y BP population. *Bone*, *15*(5), 539-545. https://doi.org/10.1016/8756-3282(94)90278-X

Lazenby, R. A., Skinner, M. M., Kivell, T. L., & Hublin, J. J. (2011). Scaling VOI size in 3D µCT studies of trabecular bone: A test of the over-sampling hypothesis. *American journal of physical anthropology*, *144*(2), 196-203. https://doi.org/10.1002/ajpa.21385

Little, N., Rogers, B., & Flannery, M. (2011). Bone formation, remodelling and healing. *Surgery (Oxford)*, *29*(4), 141-145. https://doi.org/10.1016/j.mpsur.2011.01.002

Macchiarelli, R., Bondioli, L., Galichon, V., & Tobias, P. V. (1999). Hip bone trabecular architecture shows uniquely distinctive locomotor behaviour in South African australopithecines. *Journal of human evolution*, *36*(2), 211-232. https://doi.org/10.1006/jhev.1998.0267

Messent, E. A., Ward, R. J., Tonkin, C. J., & Buckland-Wright, C. (2005). Tibial cancellous bone changes in patients with knee osteoarthritis. A short-term longitudinal study using Fractal Signature Analysis. *Osteoarthritis and cartilage*, *13*(6), 463-470. https://doi.org/10.1016/j.joca.2005.01.007

Miyakoshi, N. (2004). Effects of parathyroid hormone on cancellous bone mass and structure in osteoporosis. *Current pharmaceutical design*, *10*(21), 2615-2627. https://doi.org/10.2174/1381612043383737

Moon, H. S., Won, Y. Y., Kim, K. D., Ruprecht, A., Kim, H. J., Kook, H. K., & Chung, M. K. (2004). The three-dimensional microstructure of the trabecular bone in the mandible. *Surgical and Radiologic Anatomy*, *26*(6), 466-473. https://doi.org/10.1007/s00276-004-0247-x

Odgaard, A. (1997). Three-dimensional methods for quantification of cancellous bone architecture. *Bone*, *20*(4), 315-328. https://doi.org/10.1016/S8756-3282(97)00007-0

Odgaard, A., & Gundersen, H. J. G. (1993). Quantification of connectivity in cancellous bone, with special emphasis on 3-D reconstructions. *Bone*, 14(2), 173-182. https://doi.org/10.1016/8756-3282(93)90245-6

Otsu, N. (1979). A threshold selection method from gray-level histograms. *IEEE transactions on systems, man, and cybernetics*, *9*(1), 62-66. https://doi.org/10.1109/TSMC.1979.4310076

Pau, G., Fuchs, F., Sklyar, O., Boutros, M., & Huber, W. (2010). EBImage—an R package for image processing with applications to cellular phenotypes. *Bioinformatics*, *26*(7), 979-981. https://doi.org/10.1093/bioinformatics/btq046

Pham, D. L., Xu, C., & Prince, J. L. (2000). Current methods in medical image segmentation. *Annual review of biomedical engineering*, *2*(1), 315-337. https://doi.org/10.1146/annurev.bioeng.2.1.315

Preuschoft, H., Schönwasser K. H., & Witzel U. (2016) Selective value of characteristic size parameters in hylobatids. A biomechanical approach to small ape size and morphology. In: Reichard U., Hirai H., Barelli C. (Eds) *Evolution of Gibbons and Siamang. Developments in Primatology: Progress and Prospects*. Springer, New York.

Rafferty, K. L., & Ruff, C. B. (1994). Articular structure and function in Hylobates, Colobus, and Papio. *American Journal of Physical Anthropology*, *94*(3), 395-408. https://doi.org/10.1002/ajpa.1330940308

Raichlen, D. A., Shapiro, L. J., Pontzer, H., & Sockol, M. D. (2009). Understanding hind limb weight support in chimpanzees with implications for the evolution of primate locomotion. *American Journal of Physical Anthropology*, 138, 395–402. https://doi.org/10.1002/ajpa.20952

Räth, C., Monetti, R., Bauer, J., Sidorenko, I., Müller, D., Matsuura, M., ..., & Eckstein, F. (2008). Strength through structure: visualization and local assessment of the trabecular bone structure. *New Journal of Physics*, *10*(12), 125010. https://doi.org/10.1088/1367-2630/10/12/125010

R Core Team (2019). R: A language and environment for statistical computing. R Foundation for Statistical Computing, Vienna, Austria. https://www.R-project.org/

Roque, W. L., & Alberich-Bayarri, A. (2015). Tortuosity influence on the trabecular bone elasticity and mechanical competence. In Jorge, R. N., Tavares, J., M. (Eds) *Developments in Medical Image Processing and Computational Vision*, (pp. 173-191). Springer, Cham

Roque, W. L., Arcaro, K., & Lanfredi, R. B. (2012). Trabecular network tortuosity and connectivity of distal radius from microtomographic images. *Revista Brasileira de Engenharia Biomédica*, 28(2), 116-123. https://doi.org/10.4322/rbeb.2012.017

Ryan, T. M., & Ketcham, R. A. (2002). The three-dimensional structure of trabecular bone in the femoral head of strepsirrhine primates. *Journal of human evolution*, *43*(1), 1-26. https://doi.org/10.1006/jhev.2002.0552

Ryan, T. M., & Shaw, C. N. (2012). Unique suites of trabecular bone features characterize locomotor behavior in human and non-human anthropoid primates. *PloS one*, *7*(7). https://doi.org/10.1371/journal.pone.0041037

Scherf, H., Harvati, K., & Hublin, J. J. (2013). A comparison of proximal humeral cancellous bone of great apes and humans. *Journal of human evolution*, *65*(1), 29-38. https://doi.org/10.1016/j.jhevol.2013.03.008

Scherf, H., Wahl, J., Hublin, J. J., & Harvati, K. (2016). Patterns of activity adaptation in humeral trabecular bone in Neolithic humans and present-day people. *American journal of physical anthropology*, *159*(1), 106-115. https://doi.org/10.1002/ajpa.22835

Serra, J., *Image Analysis and Mathematical Morphology* (1982), Second Edition. Vol. 1. Academic Press, New York.

Silva, M. J., & Gibson, L. J. (1997). Modeling the mechanical behavior of vertebral trabecular bone: effects of age-related changes in microstructure. *Bone*, 21(2), 191-199. https://doi.org/10.1016/S8756-3282(97)00100-2

Sinclair, K. D., Farnsworth, R. W., Pham, T. X., Knight, A. N., Bloebaum, R. D., & Skedros, J. G. (2013). The artiodactyl calcaneus as a potential 'control bone'. Cautions against simple interpretations of trabecular bone adaptation in the anthropoid femoral neck. *Journal of human evolution*, *64*(5), 366-379. https://doi.org/10.1016/j.jhevol.2013.01.003

Sylvester, A. D., & Terhune, C. E. (2017). Trabecular mapping: Leveraging geometric morphometrics for analyses of trabecular structure. *American journal of physical anthropology*, *163*(3), 553-569. https://doi.org/10.1002/ajpa.23231

Tsegai, Z. J., Kivell, T. L., Gross, T., Nguyen, N. H., Pahr, D. H., Smaers, J. B., & Skinner, M. M. (2013). Trabecular bone structure correlates with hand posture and use in hominoids. *PLoS One*, *8*(11). https://doi.org/10.1371/journal.pone.0078781

Tsegai, Z. J., Skinner, M. M., Pahr, D. H., Hublin, J. J., & Kivell, T. L. (2018a). Ontogeny and variability of trabecular bone in the chimpanzee humerus, femur and tibia. *American journal of physical anthropology*, *167*(4), 713-736. https://doi.org/10.1002/ajpa.23696

Tsegai, Z. J., Skinner, M. M., Pahr, D. H., Hublin, J. J., & Kivell, T. L. (2018b). Systemic patterns of trabecular bone across the human and chimpanzee skeleton. *Journal of Anatomy*, *232*(4), 641-656. https://doi.org/10.1111/joa.12776

Tu, S. J., Wang, S. P., Cheng, F. C., Weng, C. E., Huang, W. T., Chang, W. J., & Chen, Y. J. (2017). Attenuating trabecular morphology associated with low magnesium diet evaluated using micro computed tomography. *PloS one*, *12*(4). https://doi.org/10.1371/journal.pone.0174806

Urbach, E. R., & Wilkinson, M. H. (2007). Efficient 2-D grayscale morphological transformations with arbitrary flat structuring elements. *IEEE Transactions on image processing*, *17*(1), 1-8. 1 https://doi.org/0.1109/TIP.2007.912582

Vala, H. J., & Baxi, A. (2013). A review on Otsu image segmentation algorithm. *International Journal of Advanced Research in Computer Engineering & Technology*, *2*(2), 387-389. https://doi.org/10.14445/22312803/IJCTT-V33P117

Venables, W. N., & Ripley, B. D. (2002) *Modern Applied Statistics with S*. Fourth Edition, Springer, Cham.

Villa, C., Hansen, M. N., Buckberry, J., Cattaneo, C., & Lynnerup, N. (2013). Forensic age estimation based on the trabecular bone changes of the pelvic bone using post-mortem CT. *Forensic science international*, *233*(1-3), 393-402. https://doi.org/10.1016/j.forsciint.2013.10.020

Witmer, L. M., Ridgely, R. C., Dufeau, D. L., & Semones, M. C. (2008). Using CT to peer into the past: 3D visualization of the brain and ear regions of birds, crocodiles, and nonavian dinosaurs. In Endo, H., Frey, R. (Eds) *Anatomical imaging* (pp. 67-87). Springer, Tokyo.

Zhou, Y., & Toga, A. W. (1999). Efficient skeletonization of volumetric objects. *IEEE Transactions on visualization and computer graphics*, *5*(3), 196-209. https://doi.org/10.1109/2945.795212.

FIGURE CAPTIONS

Figure 1 The protocol for the semi-automatic isolation of cancellous bone shown on the mandibular condyle of Hylobates lar. The region of interest (A) is cropped out of the µCT scan and the volume is binarised (B). The binarised image enters the first step of the protocol. Multiple dilations and erosions fill the empty spaces surrounding the cancellous bone, creating a mask (C) of the whole bone region. By subtracting the binary image from the mask (C minus B), the voids are highlighted (D). The voids undergo multiple dilations and erosions, returning the area occupied by voids and cancellous bone (E), which is within the compact bone. By subtracting the inside area from the mask (C minus E), the compact bone is isolated (F). The cancellous bone (G) is then obtained by subtracting the compact bone and the voids from the mask (C minus D minus F). The operation is performed on single µCT slices stacked to obtain a 3D result (H, superior and frontal views of the mandibular condyle).

Figure 2 Graphical intuition of the indices measured on the topological skeleton of cancellous bone. For ease of visualisation, the indices are shown for a 2D topological skeleton. **Node density** is represented by the number of nodes per unit area and it is calculated using a kernel density approximation over a discretised space. The **trabecular angle** (degrees) is measured between a reference axis (not shown) and the unitary resultant (red, double-headed arrow) of all trabecular directions (blue, double-headed arrows) obtained by vector sum. **Connectivity** is the mean number of branches connected to non-terminal nodes. **Tortuosity** is the ratio between the arc length of a branch and the linear distance between its starting and ending nodes (a/b). **Fractal dimension** is an index of complexity measured on the coordinates of the skeleton using the box-counting algorithm. In this approach, discrete regular grids of decreasing cell size are superimposed over the cancellous skeleton and the number of cells occupied by the skeleton are counted for each grid. Fractal dimension is the slope of the line fitting the number of cells that overlap the skeleton versus the inverse of the cell size.

Figure 3 Semi-automatic isolation of cancellous bone in the femoral head of Symphalangus syndactylus (A), the proximal humerus of Alouatta caraya (B), the distal fibula of Cercopithecus albogularis (C) and the brow ridge of Mandrillus sphynx (D). The 3D µCT scan is cut (red line) to limit the cancellous isolation to a region of interest. The results are here shown on a single 2D slice (indicated by the blue line on the 3D scan) and on the full 3D µCT stack (the cutting planes used to isolate the 3D regions of interest is shown in red)

Figure 4 Node density of the femoral head, measured using a kernel density approximation over a regular 3D grid. It is expressed as the number of nodes of the skeletonised cancellous bone per cm3. The node density is here shown for a small sample of primates over the coronal (L-M-S-I) and para-sagittal (A-P-S-I) planes. The density increases from blue to red. (A: anterior; P: posterior; S: superior; I: inferior; L: lateral; M: medial).

Figure 5 Trabecular angle of the femoral head calculated as the 3D angle between the medio-lateral axis and the resultant of all trabecular directions. Trabecular directions are measured on the branches of the skeletonised cancellous bone. The trabecular angle is here shown for a small sample of primates on a transparent model of the femoral head. The medio-lateral axis is the line perpendicular to the A-P-S-I plane (para-sagittal plane). The antero-posterior, supero-inferior and medio-lateral percentage contributions to the angle are reported. The arrow point is for easing visualisation only and does not indicate a verse. (A: anterior; P: posterior; S: superior; I: inferior)

Table 1 Complexity indices calculated on the topological skeleton of the cancellous bone in the femoral head. Standard deviation is shown only for the indices for which its calculation was possible. All indices are adimensional, except for node density and the trabecular angle. Fractal dimension is here presented as both unscaled and scaled on the height of the femoral head. For the definition and calculation of the indices, see main text.

	Mean Node Density (nodes/ cm^3)	Max Node Density (nodes/ cm^3)	SD		Trabecular Angle (degrees)		Mean Tortuosity	SD		Mean Connectivity	S
Papio	38.81	289.09	15.32		2.78		1.23	0.25		3.49	0.
Macaca	39.38	238.91	17.10		5.74		1.11	0.19		3.38	0.
Hylobates	37.99	150.73	13.12		11.59		1.29	0.36		3.22	0.
Symphalangus	36.93	228.75	14.19		4.87		1.26	0.31		3.28	0.
Gorilla	40.51	503.97	16.52		7.43		1.23	0.24		3.53	0.
Pan	47.89	472.69	15.84		12.21		1.18	0.17		3.81	1.
Human	45.51	557.71	14.93		4.61		1.21	0.21		3.86	1.

635 Figure 1

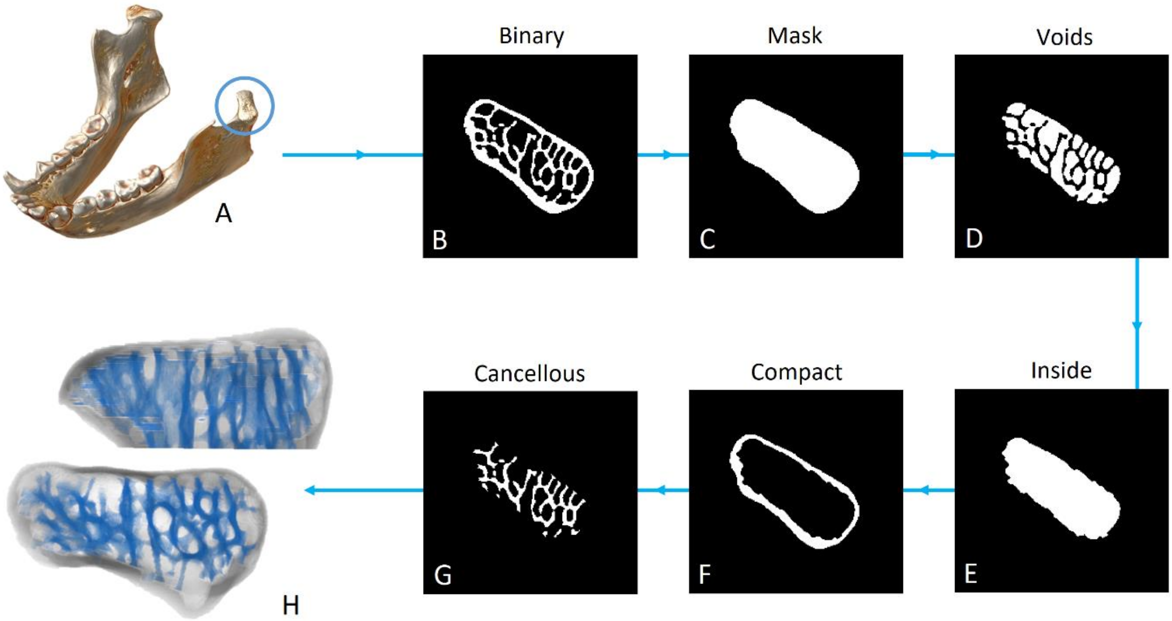

636

637

Figure 2

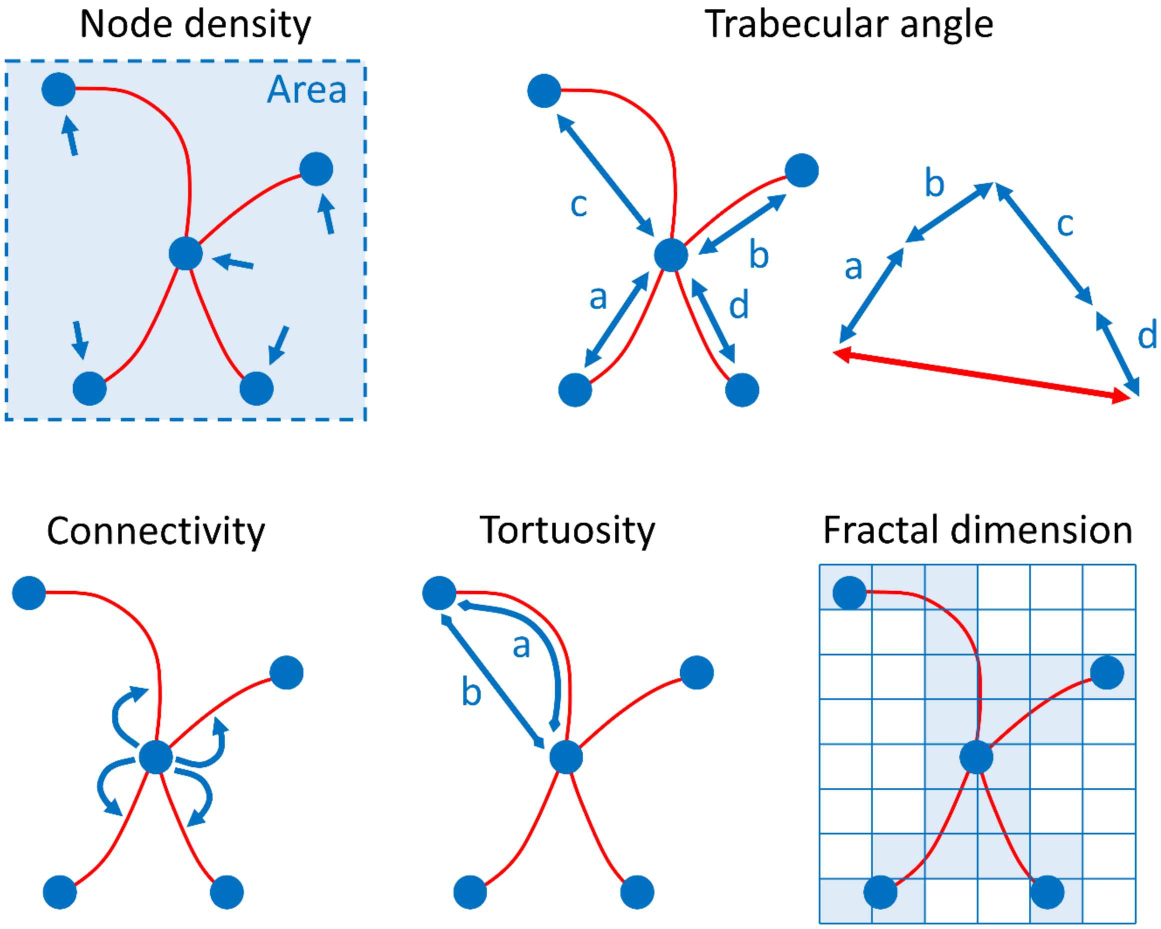
Node density
Area
Trabecular angle
c
b
a
d
b
a
c
d
Connectivity
Tortuosity
a
b
Fractal dimension

Figure 3

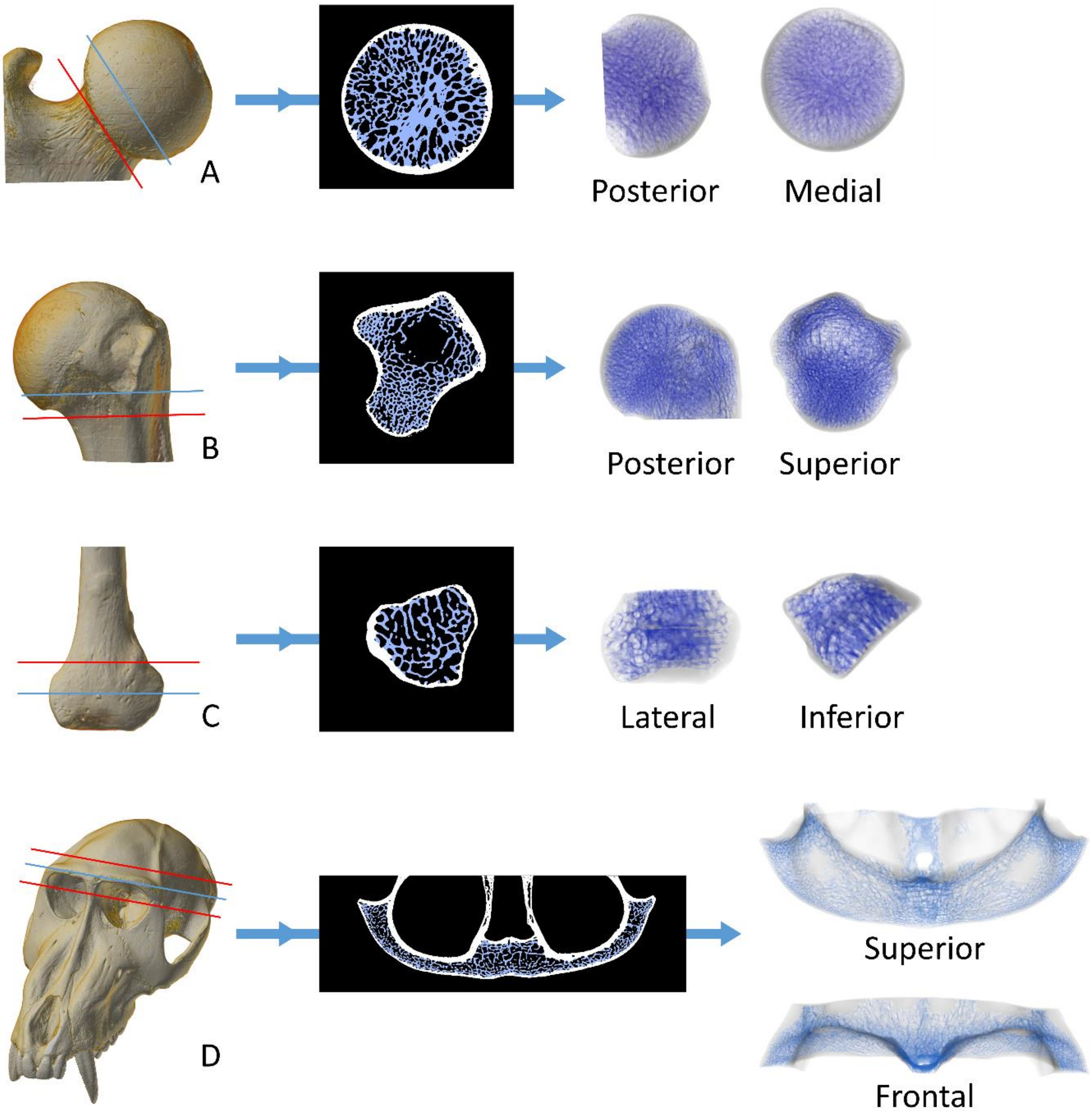
A
Posterior
Medial
B
Posterior
Superior
C
Lateral
Inferior
D
Superior
Frontal

Figure 4

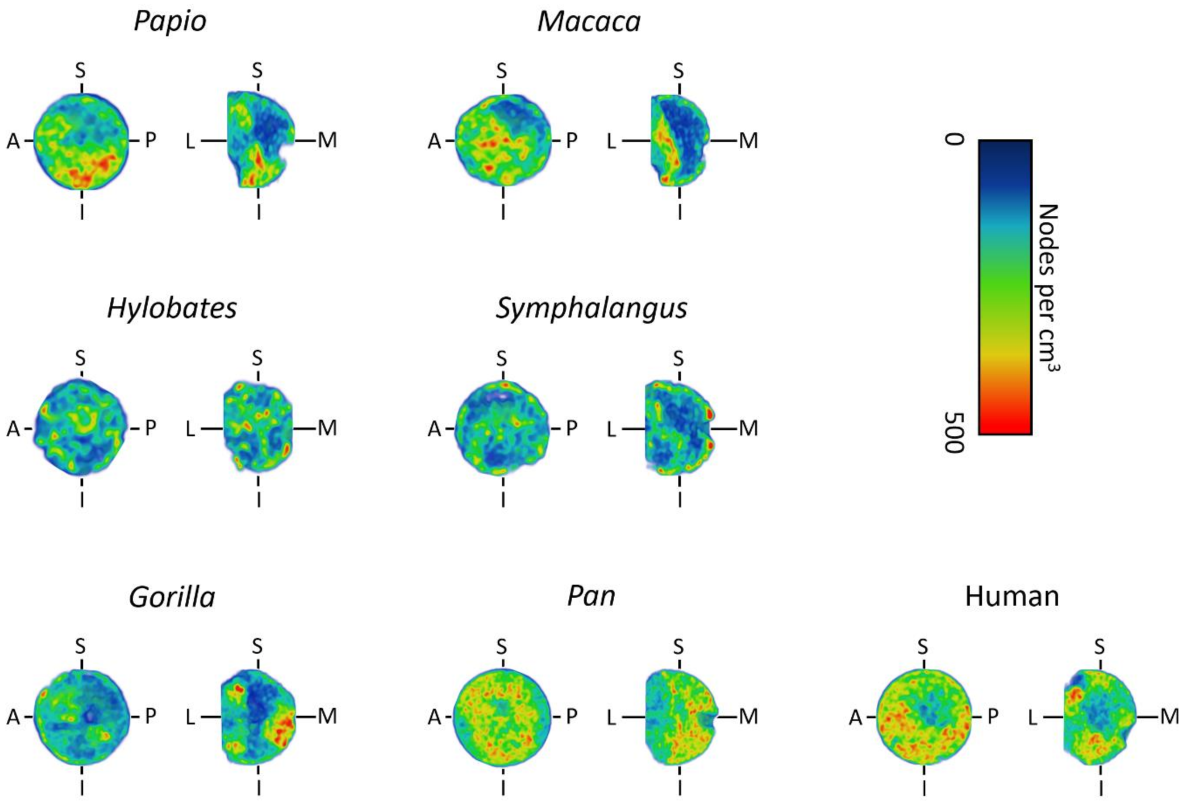
Papio
Macaca
Hylobates
Symphalangus
Gorilla
Pan
Human
S
A
P
I
L
M
0
500
Nodes per cm^3

Figure 5

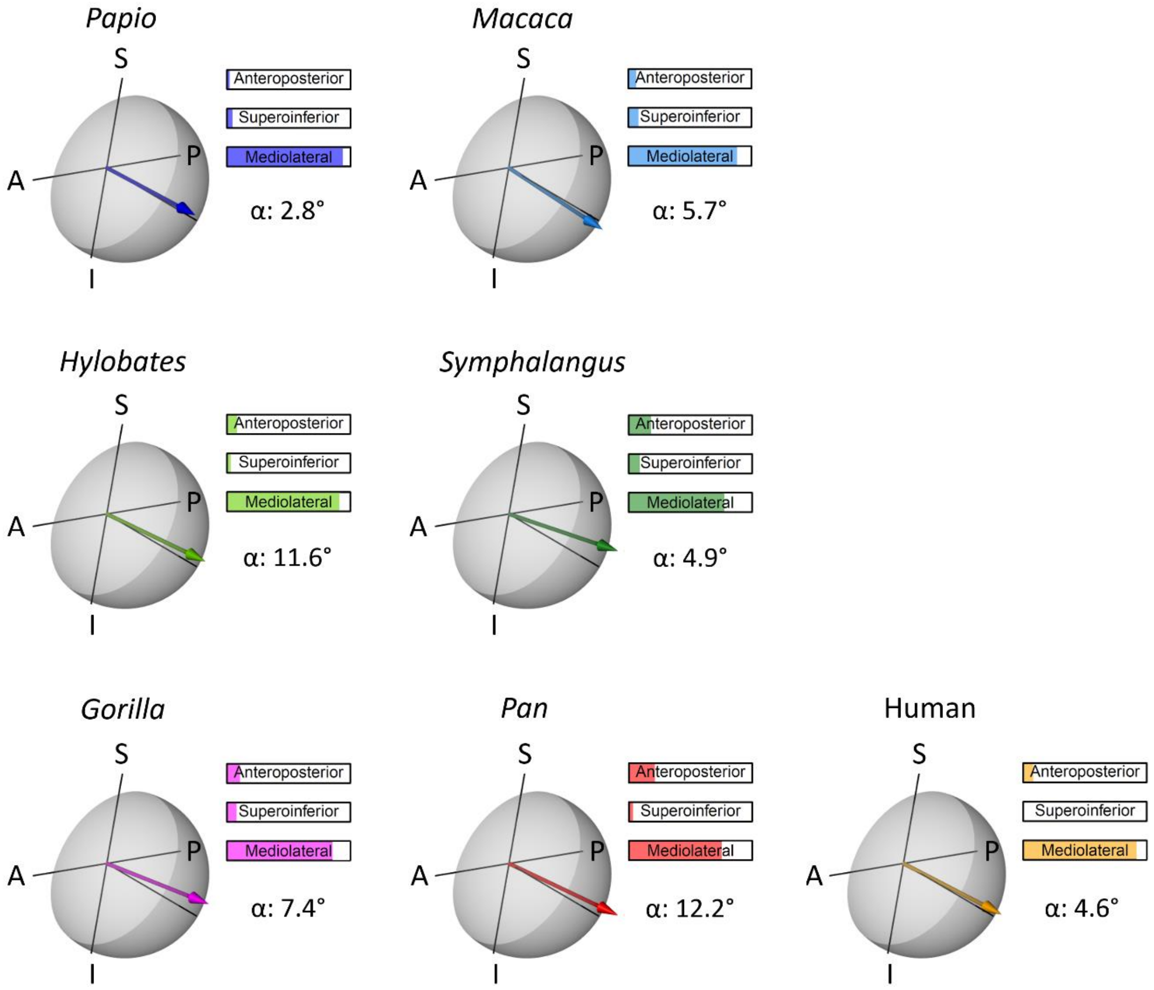
Papio
S
A
P
I
Anteroposterior
Superoinferior
Mediolateral
α: 2.8°
Macaca
S
A
P
I
Anteroposterior
Superoinferior
Mediolateral
α: 5.7°
Hylobates
S
A
P
I
Anteroposterior
Superoinferior
Mediolateral
α: 11.6°
Symphalangus
S
A
P
I
Anteroposterior
Superoinferior
Mediolateral
α: 4.9°
Gorilla
S
A
P
I
Anteroposterior
Superoinferior
Mediolateral
α: 7.4°
Pan
S
A
P
I
Anteroposterior
Superoinferior
Mediolateral
α: 12.2°
Human
S
A
P
I
Anteroposterior
Superoinferior
Mediolateral
α: 4.6°

SUPPLEMETRY ONLINE MATERIAL

Novel strategies for the characterisation of cancellous bone morphology: virtual isolation and analysis – Supplementary Information

Alessio Veneziano[1], Marine Cazenave[2,3], Fabio Alfieri[4,5], Daniele Panetta[6], Damiano Marchi[7,8]

1 Synchrotron Radiation for Medical Physics (SYRMEP), Elettra-Sincrotrone Trieste S.C.p.A., Basovizza, Trieste, Italy
2 Skeletal Biology Research Centre at the School of Anthropology and Conservation, University of Kent, Canterbury, UK
3 Department of Anatomy and Histology, Sefako Makgatho Health Sciences University, Pretoria, South Africa
4 Institut für Biologie, Humboldt Universität zu Berlin, Berlin, Germany.
5 Museum für Naturkunde, Leibniz-Institut für Evolutions- und Biodiversitätsforschung, Berlin, Germany
6 Istituto di Fisiologia Clinica, Consiglio Nazionale delle Ricerche (CNR), Pisa, Italy
7 Department of Biology, Università di Pisa, Pisa, Italy
8 Evolutionary Studies Institute and Centre for Excellence in PalaeoSciences, University of the Witwatersrand, Johannesburg, South Africa
Corresponding Author: Alessio Veneziano

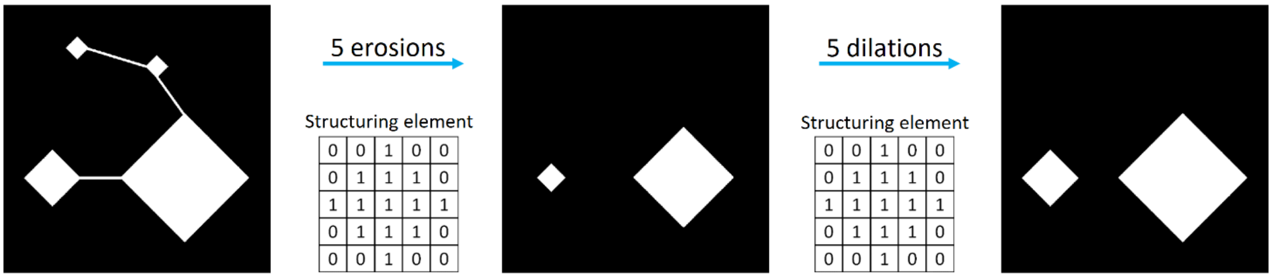

Figure S1 Action and irreversibility of Erosion and Dilation operators. The image (left) is eroded using a 5x5 diamond-shaped structuring element. The structuring element provides the operators with the transformation pattern. Dilation and erosion do not produce opposite results as they are not complementary operations. The effect of repeated dilations determines the closure of holes or flattening of concavities within an image. When such structures are lost or heavily attenuated, erosions do not restore the original appearance of the image. Similarly, when sequential erosions are applied, small components can be lost from the image and dilation does not bring them back. This situation is depicted above. After five erosions, the smaller and thinner components of the image are lost, while the large parts shrink in size (centre). Five following dilations restore the size of the large components but the small part cannot be restored (right). The irreversibility of dilation and erosion is the core of the protocol here presented as it allows losing the connections between compact and trabecular regions.

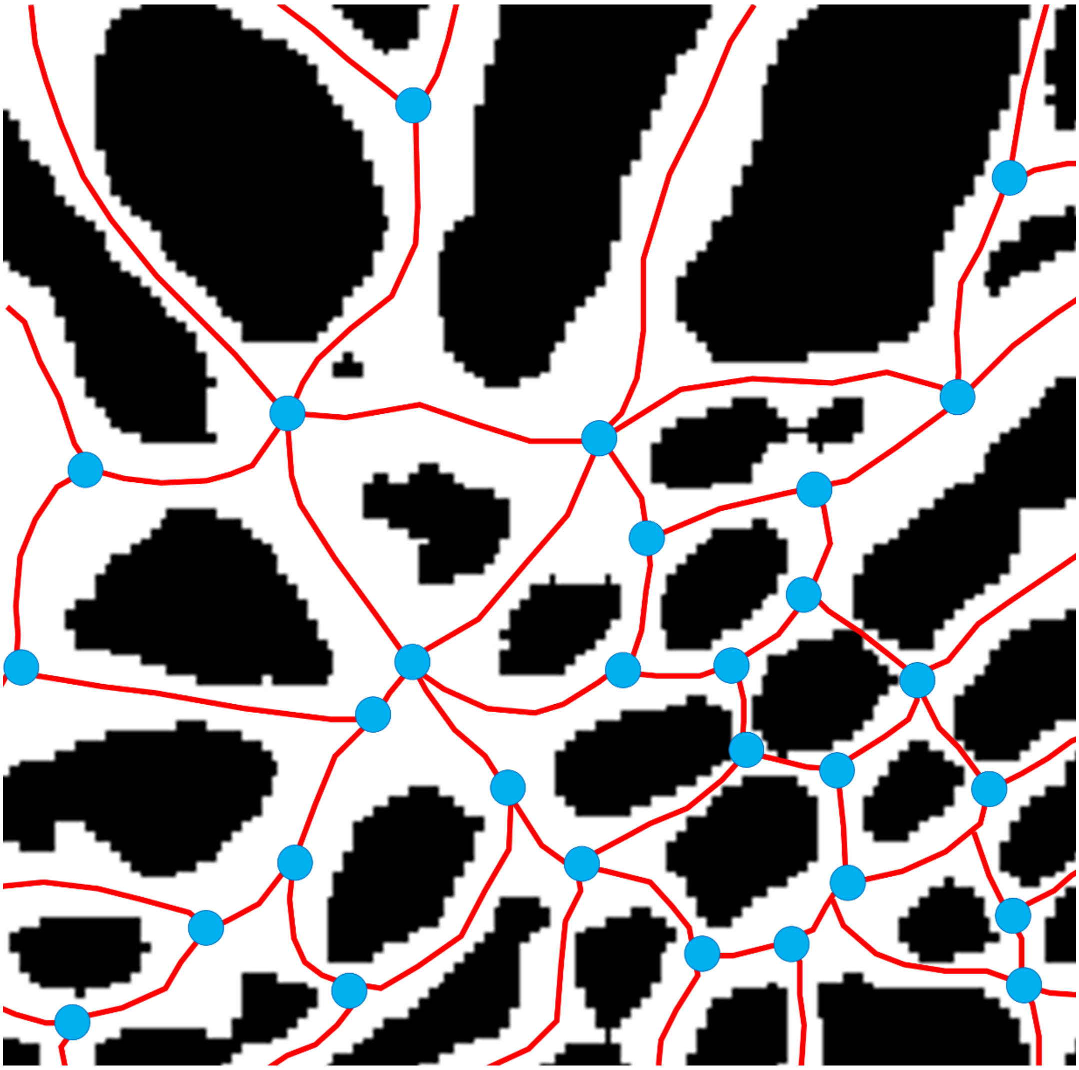

Figure S2 Skeletonisation of the cancellous bone. The cancellous architecture can be reduced to its minimal morphology by thinning the cancellous bone. The result is a lattice structure consisting of branches (red) and nodes (blue). The topological and geometric features of the skeleton can be used to measure proxies of its complexity. For the sake of visualisation, the skeletonisation is here shown on a 2D image, while for the methods presented in this paper it is performed in 3D.

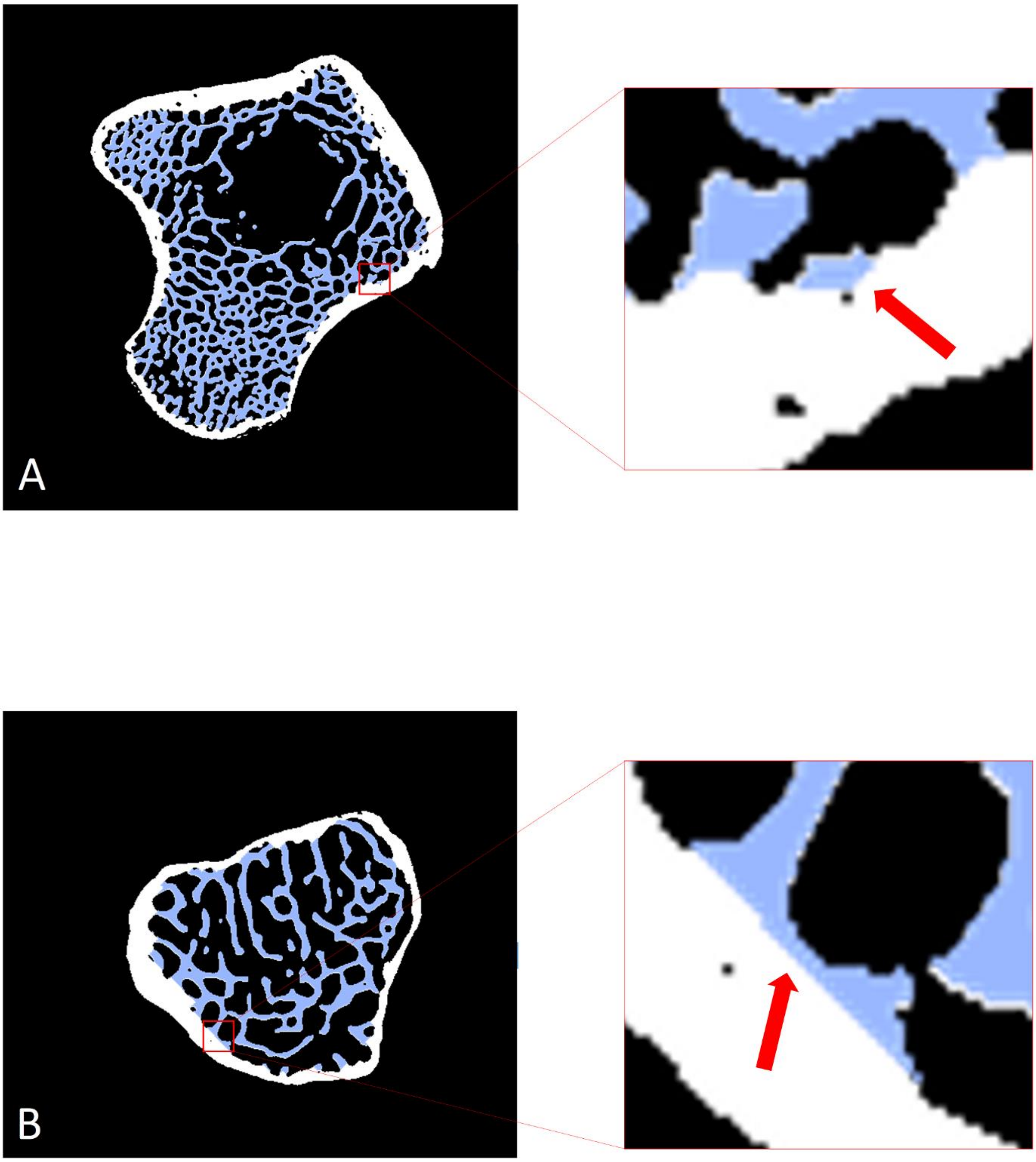

Figure S3 Details of errors that can be encountered using the isolation protocol presented in this paper. A) Detail of the isolated cancellous bone of the proximal humerus of *Alouatta caraya*. Small parts or irregularities of the internal side of the cortical bone (red arrow) can be included in the cancellous selection, in particular when close to small holes within the cortical bone. B) Detail of the isolated cancellous bone of the distal fibula of *Cercopithecus albogularis*. Bridges (red arrow) between contiguous cancellous element can be connected when the element touche the cortical bone directly. Some cortical bone can therefore be retained in the selection. These errors are usually localised to small areas and their effect on the overall calculation of cancellous statistics can be considered negligible.

Table S1 Details of the specimens (µCT) used to test the protocol of cancellous bone isolation.

Species	Skeletal region	Side	Isotropic voxel size	Source	Scanning facility
Hylobates lar	Mandibular condyle	Left	0.067 mm^3	The Museum of Comparative Zoology at Harvard University (USA)	Microfocus X-ray tomography facility, Center for Nanoscale Systems (CNS), Harvard University (USA)
Mandrillus sphynx	Brow ridge	-	0.084 mm^3	The American Museum of Natural History (USA)	Microscopy and Imaging Facility (MIF), The American Museum of Natural History (USA)
Alouatta caraya	Proximal humerus	Right	0.037 mm^3	The American Museum of Natural History (USA)	Center for Quantitative Imaging (CQI) of the Penn State University (USA)
Symphalangus syndactylus	Femoral head	Right	0.037 mm^3	The Smithsonian National Museum of Natural History (USA, courtesy of T. M. Ryan)	Microfocus X-ray tomography facility, the Smithsonian National Museum of Natural History (USA)
Cercopithecus albogularis	Distal fibula	Right	0.023 mm^3	“La Specula” Natural History Museum (Italy)	Institute of Clinical Physiology, the National Research Council (CNR-IFC), Pisa (Italy)

Table S2 Details of the femoral head sample (µCT) used to show the application of the complexity indices measured on the topological skeleton.

Species	Side	Isotropic voxel size	Source	Scanning facility
Homo sapiens	Right	0.064 mm^3	The Pretoria Bone Collection, Department of Anatomy of the University of Pretoria (South Africa)	Microfocus X-ray tomography facility (MIXRAD), the South African Nuclear Energy Corporation SOC Ltd (Necsa, South Africa)
Pan troglodytes	Left	0.041 mm^3	The Evolutionary Studies Institute, University of Witwatersrand (South Africa)	The Microfocus X-ray tomography facility, the Evolutionary Studies Institute (ESI), University of Witwatersrand (South Africa)
Gorilla gorilla	Right	0.072 mm^3	The R.A. Dart skeletal collection, University of Witwatersrand (South Africa)	The Microfocus X-ray tomography facility, the Evolutionary Studies Institute (ESI), University of Witwatersrand (South Africa)
Hylobates lar	Right	0.053 mm^3	The Museum of Comparative Zoology at Harvard University (USA, courtesy of M. Pina)	Microfocus X-ray tomography facility, Center for Nanoscale Systems (CNS), Harvard University (USA)
Symphalangus syndactylus	Right	0.037 mm^3	The Smithsonian National Museum of Natural History (USA, courtesy of T. M. Ryan)	Microfocus X-ray tomography facility, the Smithsonian National Museum of Natural History (USA)
Papio ursinus	Right	0.066 mm^3	The Department of Anatomy and Histology, the Sefako Makgatho Health Sciences University (South Africa)	Microfocus X-ray tomography facility (MIXRAD), the South African Nuclear Energy Corporation SOC Ltd (Necsa, South Africa)
Macaca fuscata	Right	0.046 mm^3	The Primate Research Institute of Kyoto University (Japan)	X-ray synchrotron radiation micro-tomography (SR-µXCT), beamline ID 17 of the European Synchrotron Radiation Facility (ESRF, France)